INTERNATIONAL JOURNAL OF HYDROGEN ENERGY 45 (2020) 20069–20079

Available online at www.sciencedirect.com

ScienceDirect

journal homepage: www.elsevier.com/locate/he

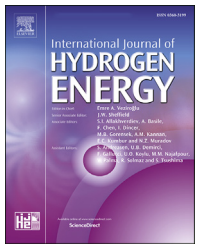

Effect of applied strain on the interaction between hydrogen atoms and $\frac{1}{2}\langle 111\rangle$ screw dislocations in α-iron

E. Luke Simpson [1], *Anthony T. Paxton* [*]

Department of Physics, Kings College London, Strand, WC2R 2LS, London, United Kingdom

HIGHLIGHTS

- Validation of the tight binding approximation for dislocation H interactions in iron.
- The role of crack tip strain field on dislocation mobility with trapped hydrogen.
- Effects of local strain fields on plastic localisation during hydrogen embrittlement.

ARTICLE INFO

Article history:
Received 18 January 2020
Received in revised form
2 May 2020
Accepted 6 May 2020
Available online 18 June 2020

Keywords:
Hydrogen
Screw dislocations
Iron
Tight binding

ABSTRACT

We address the role of hydrogen in modifying the behaviour of screw dislocations in α-iron under the influence of the tensile and compressive stresses that are expected to arise in the vicinity of a crack tip. The quantum mechanical tight binding approximation is employed to calculate the variation of the hydrogen/screw dislocation interaction with strain. The locations and binding energies of hydrogen trap-sites surrounding the unstrained core are shown to be of similar accuracy to previous *ab-initio* results. Bi-axial tension and compression is applied normal to the dislocation line; the binding energies are found to vary linearly with strain. Estimations of the effect of hydrogen in strained regions are made based on the proposition that hydrogen may both enhance the nucleation of kink-pairs by lowering the formation energy, and slow the movement of kinks by a solute drag effect. Our results suggest that these effects will be enhanced in tensile regions. The chance of hardening by the collision of crossed kinks, to form a jog, is estimated by comparing the nucleation and annihilation rate of kinks on a straight screw dislocation for a range of hydrogen concentrations and temperatures, suggesting a greatly increased incidence with tension that is accentuated at lower temperatures.

* *Corresponding author.*
E-mail addresses: Edmund.Simpson@kcl.ac.uk (E.L. Simpson), Tony.Paxton@kcl.ac.uk (A.T. Paxton).
[1] Present Address: Hephaestus Technologies, 2-8 Victoria Avenue, EC2M 4NS, London, United Kingdom

https://doi.org/10.1016/j.ijhydene.2020.05.050

Introduction

The Hydrogen Economy is becoming a reality [1]. The energy project "HyDeploy" is about to implement its first stage by augmenting the natural gas supply of Keele University with 20% hydrogen gas. This is a realisation of Northern Gas Networks' H21 project. Based on the guidelines put forth by the American Society of Mechanical Engineers (ASME) and the European Industrial Gases Association (EIGA), the addition of up to 20% hydrogen to natural gas does not greatly increase the risk of pipeline failure; however, other studies indicate that hydrogen increases this risk at proportions as low as 1% [2]. As hydrogen becomes a viable fuel for e-mobility and domestic use its interaction with pipe-work and valve gear materials needs to be fully comprehended because of the danger of the hydrogen infiltrating metal components and compromising their mechanical integrity. Furthermore, the Hydrogen Economy will require both mobile and stationary storage systems for hydrogen; conventional methods of gaseous hydrogen storage generally involve either materials that are susceptible to hydrogen damage, such as steel or aluminium canisters, or expensive materials, such as carbon fibre reinforced plastic composite [3]. In fact, the Cr–Mo steels that are commonly used for hydrogen canister manufacture can show up to an order of magnitude increase in fatigue crack growth rates when in an atmosphere of hydrogen, depending on the loading conditions [4]. This has not been a great issue because the majority of these canisters undergo relative few pressure cycles over their lifetime, generally under 25 per year [5]; however, if these canisters were to be used to fuel domestic or industrial vehicles they would be expected to withstand thousands of cycles over their lifetime. A greater understanding of the interaction between hydrogen and structural materials will then be invaluable in the development of storage solutions that provide the levels of economy and safety required for domestic use.

A great deal of effort has been directed toward the study of hydrogen embrittlement (HE) but a full understanding of the underlying mechanism is still lacking; this is due to the complexity of the problem, involving multiple time and length scales. The small mass of hydrogen also leads to a host of complications in both experiment and simulation: it has one of the highest atomic diffusivities in metals, and will exhibit strong quantum-mechanical effects at low temperature, meaning that classical treatments may not be appropriate [6]. Furthermore, it is almost impossible to image with standard experimental techniques, such as electron or x-ray diffraction or transmission electron microscopy. Generally, experimental observations are not then of hydrogen itself, but of the effects it has on the lattice; these include the observations of the effect on yield stresses, dislocation velocity, dislocation nucleation, vacancy concentration, crack-tip opening angle and so on [7–11]. The results of these experiments require interpretation that can only be provided with atomistic simulation.

Crack-tips are considered to be particularly likely sites for these mechanisms to be active, partially due to the high local concentration of hydrogen. The driving force for hydrogen diffusion is the strain gradient: in regions of high tensile stress hydrogen has a low chemical potential, and the opposite in regions of compression [12]. Hydrogen diffusion will then tend to deplete regions of compression to enhance the concentration in regions of tension; when a load is applied and a crack begins to open this will result in a redistribution of hydrogen toward the high local strain fields surrounding a crack-tip. The plastic deformation associated with the regions of high strain surrounding a crack-tip will also result in a high density of dislocations, and so a great increase in the number of trap sites available for hydrogen.

Ab-initio methods such as density functional theory provide an accurate and reliable description of atomic interactions; however, the great computational expense of these methods limits the structures that may be viably simulated, particularly when strain must be applied. Dislocations in iron have been simulated in the past by arranging the cores in a periodic array [13–15], which may not be appropriate for strained structures, or by simulating an isolated dislocation with the effect of the surrounding lattice included with some other model [16–18], which still results in great computational expense that limits the range of structures that may be simulated effectively. Tight binding is one of the simplest models that may be considered truly quantum-mechanical; it can provide both the scale and computational economy required to simulate many defect processes effectively while still providing a reliable description of hydrogen [19].

Katzarov et al. [20] employed a kinetic Monte Carlo (kMC) model to simulate the effect of hydrogen on the screw dislocation velocity in iron; this model requires energies for the effects of hydrogen on kink-trapping and kink-pair nucleation, so the rates of escape and nucleation can be calculated from transition state theory and used as input. If the variation of these effects with strain could be calculated then this model could be applied to the regions where hydrogen embrittlement is most likely to occur, i.e. the regions of high strain around a crack-tip. Estimates of the dislocation mobility variation between these local areas of tension and compression surrounding a crack tip could be invaluable to predict the conditions under which shear localisation is likely to occur. Estimation of these conditions are particularly important as it is theorised that shear localisation can lead to plastic failure: if a concentration of hydrogen atoms induce local slip then the local strain and dislocation density will increase, which will increase the local concentration of hydrogen, further reinforcing the process and possibly ultimately resulting in plastic instability.

The structure of the paper is as follows: the Theory section contains a detailed description of the theory of tight binding and charge transfer self-consistency; all of the results of this paper are then contained in Results and discussion. Within the Unstrained Case section the value of the binding energy for hydrogen in several of the strongest trap sites surrounding the easy and hard core configuration of a screw dislocation are evaluated at zero strain and compared to previous results. Biaxial strain is then applied in the plane normal to the dislocation line and the effects on the binding energies described in the Applying Strain section; these results are then employed in the Estimation of Effect on Screw Dislocation Motion section to demonstrate the variation in the effect of hydrogen on screw dislocation mobility between these strained regions.

Finally, a summary and conclusions may be found in Conclusion.

Theory

Direct-diagonalisation tight binding may be deduced as a rigorous approximation to density functional theory (DFT) [21,22]; in Kohn-Sham DFT quantities associated with an interacting system of electrons are calculated from a fictitious non-interacting system of electrons moving through an effective potential, V_{eff}, such that it shares the same density and kinetic energy as the interacting system. This non-interacting system of electrons will be described by a set of Schrödinger-like equations known as Kohn-Sham equations [23],

$$\widehat{H}\psi_n(r) = \left[-\frac{\hbar^2}{2m}\nabla^2 + V_{eff}(r)\right]\psi_n(r) = \varepsilon_n\psi_n(r) \tag{1}$$

A DFT calculation proceeds by first defining an input density, commonly taken to be a superposition of atomic charge densities, and calculating the effective potential, $V_{eff}(r)$, from it. Eq. (1) is then solved for this effective potential, which will enable the calculation of a new, output density. This comprises the first iteration of the self-consistency cycle, which is repeated until the input density matches the output to within certain tolerances, or rather that the potential matches the induced density; this output density may then be used in the density functional to calculate the energy of the system. It was demonstrated by Harris [24] and Foulkes [25] that the leading corrections to the total energy at each iteration will be second order in the difference between the input density and the exact, ground-state density. This led to the definition of a, possibly, more approximate functional for the total energy of the solid: the energy of the system is calculated from the input density alone, and no self-consistency iterations are carried out. This scheme forms the basis for the tight binding models described below and demonstrates their connection to full, self-consistent DFT.

The single-particle wavefunctions ψ_n of the system may be expanded as a set of localised atomic-orbital like basis states φ_{RL} with expansion coefficients C^n_{RL}, where R labels each atomic site by its position and $L = lm$ is a combined angular momentum index labelling each orbital type,

$$\psi_n = \sum_{RL} C^n_{RL}\varphi_{RL} \tag{2}$$

The Hamiltonian matrix elements are conceived as integrals of these basis states with the Hamiltonian operator,

$$H_{RLR'L'} = \int \varphi_{RL}(r)\widehat{H}\varphi_{R'L'}(r)dr = \langle RL|\widehat{H}|R'L'\rangle \tag{3}$$

These basis states are not necessarily orthogonal, and so may have an associated overlap matrix,

$$S_{RLR'L'} = \int \varphi_{RL}(r)\varphi_{R'L'}(r)dr = \langle RL|R'L'\rangle \tag{4}$$

The costly procedure of calculating these integrals directly is avoided in TB by constructing them from a parameterised look-up table, which may be fitted to reproduce results from experiment or more accurate methods. The Hamiltonian and overlap matrices are then made up of the elements:

$$H^0_{RLR'L'} = \begin{cases} \varepsilon_{RL}\delta_{LL'} & R = R' \\ f_{RLR'L'}(|r_{R'} - r_R|) & R \neq R' \end{cases} \tag{5}$$

$$S_{RLR'L'} = \begin{cases} \delta_{LL'} & R = R' \\ f^{ovl}_{RLR'L'}(|r_{R'} - r_R|) & R \neq R' \end{cases} \tag{6}$$

where r_R represents the coordinates of atom R. The Hamiltonian is labelled with a 0 to specify that it is the non-self-consistent input Hamiltonian, before the energy shifts associated with the self-consistency have been added. The value of the on-site energy levels and the form of the inter-site elements constitute ingredients of the model, requiring a comprehensive fitting procedure. The inter-site elements, known as hopping integrals in the Hamiltonian's case, are made up of two parts: one part that determines the dependence of the integral on bond length and one part that determines the dependence on bond angle. These integrals are generally taken to be quite short ranged, reducing to zero within the first few shells of neighbours, but their gradient will partially determine the inter-atomic forces. The functional form of this bond-length dependence must then be quite flexible, capable of being fit to reproduce previous results while still vanishing at short range with no discontinuities. These requirements are met here with the use of two functions: one fitted to reproduce the previous results, and a cutoff function that matches the value, slope and curvature at some point and then smoothly reduces it to zero at a reduced range [19,26]. The dependence on bond-angle arises from the Slater-Koster [27] convention to reduce the number of fundamental bond-integrals that require fitting; all of the combinations required for a *spd* basis are provided in their paper.

The Schrödinger equation may then be written as a linear eigenproblem and solved to obtain the state energies, ε_n, and eigenvectors, C^n_{RL} [28].

$$\sum_{R'L'} H_{RLR'L'}C^n_{R'L'} = \varepsilon_n \sum_{R'L'} S_{RLR'L'}C^n_{R'L'} \tag{7}$$

These eigenvectors may then be used to calculate the expansion coefficients of the density operator, which provides the charges, interatomic forces and bond energies.

$$\rho^{RLR'L'} = \sum_n^{\infty} f_n C^n_{RL}C^{n*}_{R'L'} \tag{8}$$

Occupancy of the eigenstates is defined by f_n, a step function at zero electronic temperature that puts the occupancy of states at two below the Fermi level and zero above. Finite electron temperatures may be simulated by replacing f_n with some smooth distribution, such as the Fermi-Dirac distribution, although this will result in an additional entropic contribution to the energy. Note that the expansion coefficients of the density operator are generally not the same as the matrix elements, the expansion coefficients are defined by:

$$\widehat{\rho} = \sum_{RLR'L'} |RL\rangle\rho^{RLR'L'}\langle R'L'| \tag{9}$$

while the density matrix elements are defined by:

$$\rho_{RLR'L'} = \langle RL|\widehat{\rho}|R'L'\rangle \tag{10}$$

The expansion coefficients will then only be equivalent to the matrix elements in the case of orthonormal orbitals.

A non-zero overlap will result in bond charge between atoms, which must be included in the Mulliken population assigned to each orbital [29]:

$$q_R = \sum_L q_{RL} = \sum_{LR'L'} \rho^{RLR'L'} S_{R'L'RL} \tag{11}$$

The tight binding bond model approximates the difference in energy between the condensed and free atom states [21], or the binding energy of the system:

$$E_{bind} = \mathrm{Tr}\left(\rho - \rho^0\right)\widehat{H}^0 + E_{clas}^{bond} \tag{12}$$

ρ^0 generally represents a superposition of non-interacting free atomic charge densities; the first term then arises from the bonding and charge redistribution in forming the solid. E_{clas}^{bond} is a classical term intended to balance the attractive first term; it may be fit to reproduce structural properties, such as the elastic constants or lattice parameter. It was demonstrated by Sutton et al. [21], with the use of the first order density functional defined by Harris [24] and Foulkes [25], that E_{clas}^{bond} represents the change in electrostatic energy (including all electron-electron, electron-ion and ion-ion electrostatic interactions) and the exchange and correlation energies as the atoms are condensed, and that these terms may be well approximated by a pair potential, provided that ρ^0 is indeed a superposition of free atomic charge densities.

The force on each atom may be obtained by making use of the Hellmann-Feynman theorem [30,31] to differentiate the binding energy with respect to atomic position. The pair-potential will also contribute to the force, but its analytic form will make the gradient trivial to obtain. The total force acting on atom R is,

$$F_R = -2\sum_{LR'L'} \rho^{RLR'L'} \frac{\partial H_{R'L'RL}}{\partial r_R} + 2\sum_{LR'L'} E^B_{RLR'L'} \frac{\partial S_{R'L'RL}}{\partial r_R} - \frac{\partial E_{clas}^{bond}}{\partial r_R} \tag{13}$$

where $E^B_{RLR'L'}$ represents the band energy, broken into orbital contributions [32]:

$$E^B_{RLR'L'} = \sum_n^{\infty} f_n C^n_{RL} C^{n*}_{R'L'} \varepsilon_n \tag{14}$$

Charge transfer self-consistency was employed for these simulations; it enables the description of charge-transfer between atoms and the interaction between the point charges accumulated on each atom [33,34]. The on-site self-interaction of the atomic charge is represented by the Hubbard potential,

$$V^U_R = \delta q_R U_R \tag{15}$$

The Hubbard U_R will be another parameter to be chosen for each species: a greater U will incur a greater energy cost for the accumulation of charge on any one site, and indeed the local charge neutrality approximation could be taken as the limit of having an infinite U. The inter-site interaction between these charges will then be represented by a Madelung potential,

$$V^M_{R0} = \sum_{\substack{R' \\ R' \neq R}} \sqrt{4\pi}\, \frac{\delta q_{R'}}{|r_R - r_{R'}|} \tag{16}$$

where the potential is labelled with a subscript 0 to denote that it is restricted to the monopole moment. The updates to the Hamiltonian arising from these potentials will be strictly diagonal and will have the form,

$$H'_{RLRL} = \frac{e^2}{\sqrt{4\pi}} V^M_{R0} + V^U_R \tag{17}$$

This will result in a second order contribution to the energy, representing all of the electron-electron interactions:

$$E_2 = \frac{1}{2}\sum_R \left(\frac{e^2}{\sqrt{4\pi}} \delta q_R V^M_{R0} + \delta q_R V^U_R\right) \tag{18}$$

Finally the force on an atom R due to these inter-site electrostatic interactions will be given by:

$$F^M_R = -\frac{e^2}{\sqrt{4\pi}} \delta q_R \nabla_{r_R} V^M_{R0} \tag{19}$$

The Stoner theory of itinerant ferromagnetism [35] may be employed to include magnetic effects, resulting in two spin-polarised Hamiltonians and an additional contribution to the energy. The Hamiltonian increments and 2^{nd} order contributions to the energy for a magnetic polarisable ion tight binding model [32] would then have the form,

$$H'_{RLRL} = \frac{e^2}{\sqrt{4\pi}} V^M_{R0} + \left(\left(U_R - \frac{1}{2}I_R\right)\delta q_R \pm \frac{1}{2} I_R m_R\right)\Big) \tag{20}$$

$$E_2 = \frac{1}{2}\sum_R \left(\frac{e^2}{\sqrt{4\pi}} \delta q_R V^M_{R0} + \left(\left(U_R - \frac{1}{2}I_R\right)\delta q_R^2 - \frac{1}{2} I_R m_R^2\right)\right) \tag{21}$$

Note that in this case there is an additional contribution to the potential and energy from the Stoner terms that acts to reduce the Hubbard on-site interactions; this represents the degree to which the on-site Coulomb repulsion is reduced for electrons with like spins due to exchange [32].

In the case of non-orthogonal orbitals there will also be off-site contributions to the Hamiltonian due to the presence of bond charge [32],

$$H'^M_{RLR'L'} = \frac{1}{2} O_{RLR'L'}\left(V^M_{R0} + V^M_{R'0}\right) \tag{22}$$

$$H'^U_{RLR'L'} = \frac{1}{2} O_{RLR'L'}\left(V^U_R + V^U_{R'}\right) \tag{23}$$

where $O = S - I$; this term is then identical to the overlap matrix S except with zeroes along the diagonal. This will result in additional contributions to the forces [32],

$$\partial\rho^S_{RR'} = \sum_{LL'} \rho^{RLR'L'} \frac{\partial S_{RLR'L'}}{\partial r_R} \tag{24}$$

$$F^M_R = -\sum_{R'} \left(V^M_{R0} + V^M_{R'0}\right)\partial\rho^S_{RR'} \tag{25}$$

$$F^U_R = -\sum_{R'} \left(V^U_R + V^U_{R'}\right)\partial\rho^S_{RR'} \tag{26}$$

$\partial\rho^S$ is a quantity defined in Ref. [32]. The origin of these forces can be understood by considering a pair of atoms moving relative to each other in a system: as the separation of the atoms changes so will their overlap, and so the bond charge that can be attributed to each atom. It is this change in charge, and so Hubbard potential, that gives rise to the Hubbard contribution to the force. The changing bond charge will also change the monopole moment on each atom, and so the Madelung contribution arises from the change in electrostatic interaction between these two sites and all other sites.

Results and discussion

Unstrained Case

The basis set used for these simulations was a *sd*-non-orthogonal parameter set for iron and hydrogen, fitted for direct-diagonalisation TB by Paxton and Elsässer [19]. A disk of radius 25 Å and containing 388 atoms was generated so that it was normal to the $[11\bar{1}]$ direction (taken to be the *z*-axis), and had a periodicity along this direction of a single Burgers vector. The atoms were then displaced according to the solutions of the anisotropic elasticity equations in order to introduce a screw dislocation with either the easy core configuration (ECC) or the metastable hard core configuration (HCC) [36]. A 5 Å wide layer of atoms around the rim of the cell was frozen, to negate the large forces associated with the surrounding vacuum, while the rest were relaxed using the Fletcher-Powell algorithm until the maximum force was less than 10^{-4}eVÅ^{-1} [37]. A disk of radius 13 Å was then cut out from the centre of this cell and stacked three times, which was found to be the minimum number required for the hydrogen-dislocation binding energies to converge to within 10^{-4}eV, and so did not have significant interaction between the periodic images of the hydrogen atom. Again, a 5 Å wide layer of atoms around the rim of the cell was frozen. The bottom three atoms of each screw core in the triple layer cell were frozen along z in order to prevent the screw moving with the introduction of hydrogen, which was placed in several of the binding sites found by Itakura et al. [17]. The Methfessel-Paxton sampling method was used for the Brillouin zone integration, using $1\times 1\times 24$ and $1\times 1\times 16$ *k*-point divisions for the large, single-layer cell and the small, three-layer cell respectively [38].

The dissolution energy is defined here as the difference between the total energy of the crystal with hydrogen within it and that of the crystal alone added to the energy of hydrogen in vacuum [39],

$$E_s = E_{d+H} - E_d - \frac{1}{2}E_{H_2} \tag{27}$$

where E_{d+H} is the energy of the cell containing the dislocation and a hydrogen in a binding site around it, E_d is the energy of the cell containing just the dislocation and E_{H_2} is the energy of molecular hydrogen, taken to be −4.75eV [40]. This is an approximation, taking the system to be at zero temperature and pressure; the dissolution energy should be calculated as the change in free energy with hydrogen dissolution and so E_{H_2} should be the chemical potential of hydrogen. The binding energy will then be the difference between this dissolution energy and the dissolution energy of hydrogen in a bulk tetrahedral site, so that a more positive value indicates stronger binding,

$$E_{\text{bind}} = (E_{d+H} + E_P) - (E_d + E_{P+H}) \tag{28}$$

where E_P represents the energy of a cell of the perfect lattice with an equal number of Fe atoms, and E_{P+H} is the same cell with a hydrogen atom in a tetrahedral site. This equation shows clearly that the binding energy is equivalent to the energy change in going from a perfect crystal with hydrogen and one containing a dislocation to having all the hydrogen in the dislocation cell and none in the perfect crystal. Note that the value of E_{H_2} is arbitrary when calculating the binding energy as it cancels out.

Due to the small mass of hydrogen it is important to include quantum effects; the correction arising from zero-point vibrations was calculated for each binding site. Again following Itakura et al., it was assumed that the zero-point energy (ZPE) correction could be approximated with the motion of the hydrogen atom only, assuming that the localised hydrogen vibrational modes would be decoupled from the lattice vibrations due to the large difference in mass. The hydrogen atom was displaced 0.015 Å in the ±x , ±y and ±z directions and the change in forces used to construct the Hessian matrix as the 1st order central finite difference. The normal mode frequencies can then be obtained from the mass-weighted eigenvalues of the 3×3 Hessian matrix,

$$\nu_i = \frac{1}{2\pi}\sqrt{\frac{k_i}{m_H}} \tag{29}$$

where m_H is the mass of the hydrogen atom and k_i are the eigenvalues of the Hessian matrix. These frequencies can then be used to calculate the ZPE correction,

$$E_z = \frac{1}{2}\sum_{i=1}^{3} h\nu_i \tag{30}$$

where *h* represents the Planck constant.

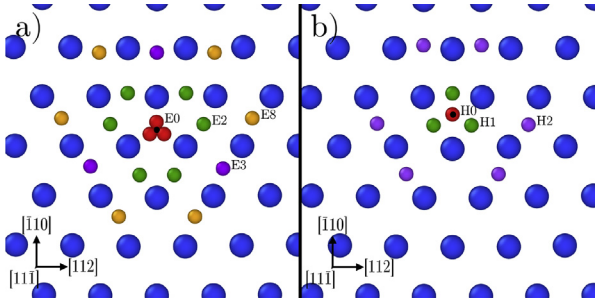

Fig. 1 – The positions of the strongest hydrogen trap-sites around a $\frac{1}{2}\langle 111\rangle$ screw dislocation of a) easy and b) hard core configuration. Iron atoms are represented with blue circles, the elastic centre of the screw core is marked with a black circle, and the other colours represent trap-sites. Due to the three-fold symmetry of the screw core, each trap will have 1,3 or 6 identical sites around the dislocation core. (For interpretation of the references to color in this figure legend, the reader is referred to the Web version of this article.)

Table 1 – Shown (in meV) are the dissolution energies (E_s), binding energies (E_b), ZPE corrections (E_z) and the corrected binding energies (E_b^z) for hydrogen in the bulk tetrahedral site and several sites around the ECC and HCC screw dislocation. Figures in brackets are the equivalent results from Itakura et al. [17].

Site	E_s	E_b	E_z	E_b^z
Tet.	233 (241)	0 (0)	219 (238)	0 (0)
E0	114 (156)	119 (85)	213 (224)	126 (99)
E2	7 (30)	227 (185)	152 (167)	294 (256)
E3	99 (103)	134 (138)	153 (175)	200 (201)
E8	203 (195)	30 (46)	163 (207)	86 (77)
H0	−29 (−71)	263 (286)	94 (134)	388 (390)
H1	−43 (−56)	276 (271)	161 (187)	335 (322)
H2	73 (116)	160 (125)	149 (174)	230 (189)

The positions of the trap-sites simulated are shown in Fig. 1; the resulting energies are shown in Table 1, alongside the equivalent energies calculated by Itakura et al. with GGA DFT [17]. The binding sites for the hydrogen were found to be in the same positions as those found by Itakura et al. [17]. The E2 site was also found to match with that defined in Zhao and Lu [16], who used a quantum-mechanics/molecular-mechanics (QM/MM) approach with a core of DFT to simulate hydrogen around a screw dislocation. As shown in Table 1, all of the results from TBE are found to be in excellent agreement with the DFT results, every one within the estimated error stated by Itakura et al. apart from E2, which was beyond the ±32meV error range by 6 meV, but still close to the value of 270 meV found by Zhao and Lu. The ZPE correction is also shown to be essential in this case as it is required to correct the ordering of the H0/H1 binding strengths. Gibala et al. [41] carried out similar calculations to Itakura et al., using GGA DFT with Green's function boundary conditions, but found lower binding energies for these sites: they calculated the E0 site to have a binding energy of only 60 meV, while the E1 site (which Itakura et al. found to be part of the same energy basin as the E2 site and to have a similar energy) had a binding energy of only 170 meV. They also found that two pyramidal sites, separated by 1.5 Å and 2 Å from the dislocation core respectively, had very slightly stronger binding energies than the E2 site. It is interesting to note that Ramasubramaniam et al. [42] were able to obtain the correct position for the E2 site, and a similar binding energy of 240/270meV, using two interatomic potentials fitted to DFT results and experimental data; however they also found a fictitious stronger binding site for the ECC located between each of the three core atoms, where H1 would be located if the screw was HCC. Our ZPE-corrected dissolution energy of hydrogen in a tetrahedral was also found to match well with previous results: the value calculated here of 319 meV is in excellent agreement with previous DFT estimates of 301 meV [39] and 330 meV [43], and an experimental estimate of 296 meV [44].

Applying Strain

In order to observe the variation of binding energy with strain, biaxial tension and compression was applied in the *xy*-plane (normal to the dislocation line). Biaxial strain was applied instead of hydrostatic so that the results would be directly comparable between different levels of strain: interaction between the hydrogen atom and its images could become a factor if compression was applied along z, not to mention the interaction with the frozen core atoms. Strain along z is then neglected and the approximation is made that these results are similar to those that would be obtained for the hydrostatic case. The strain was imposed on the single layer cell incrementally in units of 0.1%; the cell was then relaxed, stacked again and re-relaxed with hydrogen. The values for the bulk tetrahedral site dissolution and the ZPE correction for each site were also recalculated at each value of the strain.

Shown in Fig. 2(a) and (b), as a function of compressive and tensile biaxial strain in the plane normal to the dislocation line, are the ZPE-corrected binding energies relative to a strained tetrahedral site and ZPE-corrected binding energies relative to an unstrained tetrahedral site respectively. The variation of dissolution energy for each site with strain is shown to be fairly linear with some minor variation, increasing with compression and decreasing with tension as found by Ramasubramaniam et al. [43] using GGA-DFT for a tetrahedral site under hydrostatic strain.

The variation of the binding energies in graph (a) has the opposite pattern to those in graph (b); this is due to the fact that the gradient of the tetrahedral site dissolution energy was greater than that for other sites, and so the tetrahedral dissolution energy approaches the others with tension and diverges with compression. This would then have the effect at equilibrium that a slightly greater proportion of the local concentration of hydrogen would be segregated to screw dislocations in compressive regions than tensile; however, there would be a greater local concentration in tensile regions as the binding to tetrahedral sites is greater. The actual effect of this variation is difficult to assess, and may depend on how long the system has to equilibrate between kink nucleation or movement events, but only the case of a system in full equilibrium will be considered here.

In fact, the gradient of the dissolution energy for every site was found to be roughly proportional to their value; so those sites with a large dissolution energy, and so weak binding, also had a large variation with strain, while those with a stronger

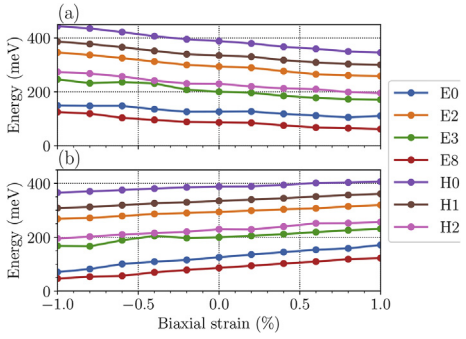

Fig. 2 – Variation of (a) ZPE-corrected binding energy relative to a strained tetrahedral site and (b) ZPE-corrected binding energy relative to an unstrained tetrahedral site for the strongest hydrogen trap sites around ECC and HCC screw cores with biaxial tensile or compressive strain applied in the plane normal to the dislocation line.

binding had a smaller variation. The strongest binding site, H0, had the smallest gradient, with a variation of 41meV between 1% tension and compression, while E0 is the second most weakly bound has a variation of 101meV and the tetrahedral site has a variation of 121meV across the range of strains. This is a fairly weak effect but would mean that the energy landscape for hydrogen around the screw core would become slightly more or less rugged with compression and tension respectively, which may slightly alter the effect that the presence of hydrogen has on the energetics of screw processes.

Estimation of Effect on Screw Dislocation Motion

When a kink-pair is nucleated on a screw dislocation line a section of the line moves forward one Peierls valley, passing close to the HCC in the process; Itakura et al. calculate the change in enthalpy for this process by considering the hydrogen to remain stationary during the transition, a fair assumption for the E2 site in front of the dislocation line as it is strongly bound throughout. The hydrogen in this site moves relative to the dislocation core through the sites E2-H0-E2 during the transition, showing an increase in binding energy from E2 to H0 of 94meV at 0% strain and so reducing the enthalpy for the process; this binding energy change shows a very slight variation with strain, increasing by only 3meV with 1% compression and decreasing by 7meV at 1% tension.

Strain will also have a slight effect on the kink-trapping by hydrogen: as the time scale for kink migration is much shorter than that for hydrogen diffusion the hydrogen will remain essentially stationary as the kink sweeps past and moves the dislocation line one Peierls valley relative to the hydrogen atom, therefore a decrease in hydrogen binding energy will act to trap the kink. The largest kink trap energy for hydrogen behind the dislocation line would come from hydrogen that follows the path of E2-H2-E8 relative to the screw core as the kink sweeps past, which would have a total decrease in binding energy, or kink-trapping energy, of 207meV at 0% strain. This shows an increase of 14meV at 1% compression and a decrease of 11meV at 1% tension. Finally the other kink-trapping energy would come from the path E2-H2-E3 which shows a weaker trapping effect of 94meV at 0% and changes of ±6meV at 1% compression and tension respectively. The weaker binding energies of the E3 and E8 sites would result in lower occupancy and so any transition with the hydrogen initially in these sites is unlikely to have a large effect.

It may be easier to see the effect of hydrogen on screw dislocation mobility by considering the variation in average kink velocity with hydrogen bulk concentration. Katzarov et al. [20] estimated the velocity at which a kink would travel past a hydrogen atom in their kMC model from the transition state theory expression for the rate at which the kink could escape each hydrogen trap,

$$P_H = f_k \exp\left(-\frac{E_t(\sigma)}{k_B T}\right) \tag{31}$$

$E_t(\sigma)$ in this case represents the stress-reduced hydrogen kink-trapping energy, which Itakura et al. estimated using the string method at various values of applied shear; the $E_t(\sigma)$ used here was obtained by fitting a cubic spline to their results and then scaling it such that it matched the value for each strain calculated here at zero effective shear stress (E_t^0). The attempt frequency f_k is taken to be the Debye frequency for iron ($f_k = 1.34 \times 10^{13} s^{-1}$), k_B represents the Boltzmann constant and T the temperature. However, this would not include the chance that kinks could jump back into the hydrogen trap immediately after escaping; Katzarov et al. estimate this chance from the forward and backward jump frequencies from the kink position directly after the trap, or J_k^+ and J_k^- respectively,

$$J_k^+ = f_k \exp\left(-\frac{\Delta E - \sigma b^2 h}{k_B T}\right) \tag{32}$$

$$J_k^- = f_k \exp\left(\frac{E_t(\sigma) - \sigma b^2 h}{k_B T}\right) \tag{33}$$

ΔE represents the energy change as the kink moves forward, from elastic interactions with other kinks and so on; in the simplified estimates made here this contribution will be approximated to be zero, so the kinks described here are essentially moving along a straight dislocation with no surrounding defects. The modified escape-rate is then,

$$P_H^+ = P_H \frac{J_k^+}{J_k^+ + J_k^-} \tag{34}$$

which may then be employed to estimate the velocity with which a kink would pass a hydrogen atom, from the expression for the kink mobility [45],

$$v_k^H = \frac{\sigma b h}{k_B T} b^2 P_H^+ \tag{35}$$

The barrier to kink motion without solute drag is so low in iron that it does not require thermal fluctuations to overcome it, even at low applied stresses (estimated to be between 5×10^{-5}eV and 9×10^{-5}eV) [46]. Therefore, if it does not encounter hydrogen or other defects, its velocity will only be limited by phonon drag, or lattice damping resistance, which may be characterised by the coefficient $B_k(T)$ [47]. In this case the kink velocity will be inversely proportional to this phonon drag coefficient and the effective stress on the dislocation,

$$v_k = \frac{\sigma b}{B_k(T)} \tag{36}$$

The most reliable way to estimate the phonon drag coefficient is to observe the mobility of individual dislocations with applied stress; B_k will then be inversely proportional to the gradient of the steady state velocity of the dislocation with stress. Kuksin and Yanilkin [48] used MD simulations with an interatomic potential for iron to obtain values for $B_k(T)$ at a range of temperatures, observing a fairly linear dependence of $B_k(T) = (2.7 + 0.008T) \times 10^{-5}$Pas. This relation for the phonon drag coefficient will be used here; although Kuksin and Yanilkin also found that $B_k(T)$ increased with hydrostatic compression, the change was by less than 2% at 1% compression and so this variation will not be included. The concentration (C_b) of hydrogen in each binding site of strength E_b^z with a hydrogen lattice concentration C_0 can be estimated from the McLean isotherm,

$$C_b = \frac{\frac{1}{6}C_0 \exp(E_b^z/k_B T)}{1 + \frac{1}{6}C_0 \exp(E_b^z/k_B T)} \quad (37)$$

where the concentration C_0 is divided by six in order to convert it from atomic parts per million to the number of solutes per site, and there are six tetrahedral sites per iron atom. The reduced velocity of the kinks due to the presence of hydrogen can then be estimated from these two velocities as $v'_k = C_b v_k^H + (1 - C_b)v_k$; Results for several values of effective shear at a temperature of 300 K are shown in Fig. 3.

Due to the small secondary Peierls barrier, normal kink motion is very fast and even the lowest concentration of hydrogen reduces the kink velocity to a small proportion of its original value at $\sigma = 30$MPa. However, even the lowest reduced velocity calculated here is still $\sim 3 \times 10^{-2}$ms^{-1} (for $C_0 = 10$appm at $\sigma = 30$MPa), a large value relative to the length of dislocations, which would be on the order of micrometers. This velocity is only decreased to 7×10^{-6}ms^{-1} at a lower stress of $\sigma = 1$MPa. Kink-trapping becomes less effective as the effective shear stress is increased, and so the velocity at all applied strains and hydrogen concentrations increases as a proportion of v_0. In general, it can be seen that this drag is much more effective in regions of tension, but if the stress is sufficient to free the kinks from hydrogen trapping then the effect is reduced and the velocity is almost constant across the applied strains.

It should be noted that the kink velocity will not directly determine the degree of hardening, i.e. the reduction in plasticity, unless the movement and annihilation of kinks is the rate-limiting step in dislocation motion. Kink-pair nucleation is a rare event with a high activation energy and, if the embryonic kink-pair does not quickly separate beyond a critical width, then the new kinks will frequently annihilate with each other. The temperature and strains shown here were chosen to illustrate the variation in magnitude of hydrogen's effect on the kink velocity with biaxial strain; it is unlikely for the kink motion to be the rate-limiting step in these regimes.

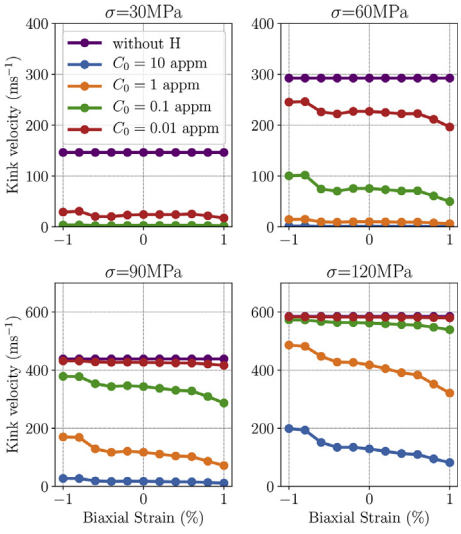

Fig. 3 – The average kink velocity against the biaxial strain at several effective shear stresses and hydrogen lattice concentrations at a temperature of 300 K.

Itakura et al. [49] calculate the stable kink-pair nucleation rate using the Arrhenius law: $R_N = D_d N_d \exp\left(-\frac{E_k(\sigma)}{k_B T}\right)$, where N_d is the dislocation length in units of b and $E_k(\sigma)$ is the stress-dependent kink nucleation enthalpy. The attempt frequency D_d was estimated from experimental measurements of the dislocation velocity at room temperature by Caillard [50], and so this rate would only refer to the nucleation of stable kink-pairs, not those that immediately annihilate after nucleation. The enhancement of the kink-nucleation rate due to hydrogen atoms in front of the dislocation line may be estimated within transition state theory as $1 + C_b W_k\{\exp(\Delta E_k/K_B T) - 1\}$; W_k here is the width of the embryonic kink-pair (found to be 10 Burgers vectors in string method [49] and tight binding nudged elastic band [20] simulations of kink-pair nucleation) and ΔE_k is the change in kink nucleation enthalpy with hydrogen in the E2 site. This enhancement factor may be arrived at by considering that a proportion of the line, given by $C_b W_k$, will have a hydrogen atom in front of the embryonic kink-pair as it is nucleated, and so will have the barrier lowered by ΔE_k. Itakura et al. [17] calculated this enthalpy change to be 110meV using a line tension model and the string method [51].

Hardening does not only occur directly from the reduction in kink velocity, but also in some situations indirectly: as the kink-pair nucleation rate is enhanced and the average kink velocity is decreased it becomes more likely that the dislocation will still have kinks travelling along it when it nucleates a new kink-pair, possibly on an another slip plane [20]. The collision of kinks on different slip planes will result in the generation of jogs: short sections of edge dislocation on a different glide plane from the rest of the dislocation. These will then form strong pinning points for the dislocation, requiring climb of the jog segment for the dislocation to move in its glide plane and so reducing its mobility. This mechanism is more likely than the kink-drag mechanism to have an effect at low hydrogen concentrations because it does not require kink-annihilation to be the rate-limiting step in order to be active, but smoothly increases in likelihood as the annihilation rate approaches the nucleation rate.

For a dislocation with a length of $2\mu m$, a kink-pair nucleation enthalpy of 595meV and under an effective stress of 33 MPa (taken from Itakura et al. [17]) the variation of kink velocity and kink-pair nucleation rate was calculated for a range of biaxial strains, hydrogen bulk concentrations and temperatures. The kink annihilation rate may be approximated by dividing the length of the dislocation by the kink velocity, then taking the kink-pair nucleation rate over the rate of kink annihilation will give an estimate of the number of kink-pairs formed while each kink travels along the dislocation line, or the chance for crossed-kinks to collide and form pinning points. The same assumptions as made in the previous calculation are made here, along with the further assumptions that the kink-pairs are nucleated both in front of and on a different glide plane to the travelling kink. Results for a range of concentrations, temperatures and strains are shown in Fig. 4.

The graphs illustrate that the chance of pinning-point formation is much greater in areas of tension, although there is some variation at the lowest and highest

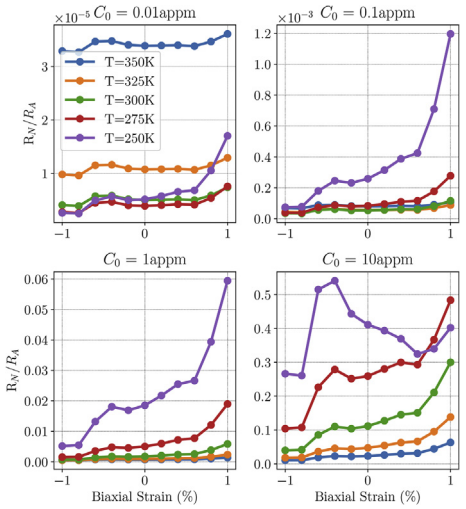

Fig. 4 – Shown for several hydrogen lattice concentrations (C_0) and temperatures (T) is the kink-pair nucleation rate (R_N) over the kink annihilation rate (R_A), which is taken as the time taken for the kink to travel the length of the dislocation. This provides an estimation of the chance of pinning-point formation for each kink-pair nucleated. The dislocation length is 2μm and the applied stress is 33 MPa.

concentrations shown. The variation in binding energy gradient results in a kink-trapping energy that is greater by at 1% compression than 1% tension by ~ 10%; also, as the bulk concentration is increased, the proportional difference in the occupation of these sites between regions of tension and compression is decreased. The exponential dependence on the trap energy means that this small variation in energy becomes more important than the concentration difference between regions after a certain point. Solute drag is then more effective in compressive zones but the nucleation enhancement is similar, so pinning point formation becomes more likely in the compressive zone. However, this effect likely only becomes active at very low temperatures and high hydrogen concentrations.

For $C_0 > 0.01$appm, every graph generally shows an increase in pinning-point formation chance as the temperature is lowered, and an increase in the gradient of the lines so that the discrepancy between tensile and compressive regions is intensified. At $C_0 = 0.01$appm, however, this trend is reversed for the highest temperatures, which show a steady increase in chance with T and little dependence on strain. This occurs because the effects of temperature on these processes become dominant over those of hydrogen: the low concentration and high temperature means that the kink velocity is determined more by phonon drag than solute drag, and the increased temperature also results in an increase of the kink-pair formation rate. This is why the lines for $T \geq 300$K are close to level across the strains. Katzarov et al. [20] also observed this trend with their kMC model: at low applied stresses ($\sigma \approx$ 50MPa) pinning-point formations at 300 K were unlikely and required concentrations of $C_0 > 0.5$appm, but the chance increased greatly at 400 K, with no hydrogen, because the nucleation of kink-pairs on different glide planes became more likely.

Conclusion

A cylindrical cell containing an isolated screw dislocation in α-Fe was used to calculate the binding energy for hydrogen to several of the strongest sites surrounding the dislocation. The advantage of using tight binding for these calculations was that it could provide both the quantum-mechanical accuracy required to give a valid description of hydrogen and the scale required to determine the structural variation of the core with strain. These binding energies were found to have a similar accuracy to previous DFT simulations at zero strain: almost every value was within the error bounds set by Itakura et al. [17] for their DFT results, apart from that for the E2 site which exceeded the bounds by 6meV.

These cells were then used to assess the variation in screw-hydrogen binding energy in regions of high compressive and tensile strain, as might be found around a crack tip. The binding energy of the sites relative to a tetrahedral site under the same strain were found to increase with compression; the opposite trend for the binding energies relative to an unstrained tetrahedral site. This could possibly result in a greater proportion of the local hydrogen concentration being segregated to screw dislocations in regions of compression; although the local hydrogen concentration would be greater in regions of tension. It was also found that the relative depths of the binding sites around the screw dislocation should converge slightly with tension; this would result in a slight decrease in the effect of a hydrogen atom on screw dislocation motion, whether by kink-trapping or reducing the energy for kink-pair formation enthalpy. The variation was found to be around ±5% of the energy difference between binding sites, that would result in kink-trapping or kink-pair formation enthalpy reduction, with ±1% biaxial strain respectively.

These results were then used to carry out several calculations to give an indication of the variation in hydrogen effect on screw dislocation mobility between regions of tension and compression. The average kink velocity was estimated from the velocity with which kinks would pass a hydrogen atom, estimated with the escape rate from hydrogen traps, and the unimpeded velocity for a range of effective shear stresses and hydrogen concentrations. The velocity was found to be greatly reduced even for low hydrogen concentrations and again showed a large difference between regions of tension and compression; however, even the lowest values calculated were still large in terms of the length of a dislocation. In general, it was also found that the difference between regions of tension and compression was decreased under higher effective stresses, as the kinks could escape the hydrogen traps more easily.

This same dislocation was then used to estimate the number of kink-pair nucleation events that could occur while kinks are still travelling along the dislocation line, or the number of potential pinning points that could be formed from kinks on different glide planes colliding per kink-pair nucleation. This was found to be a complex, multivariate problem, dependent on both the degree of kink-trapping and kink-pair nucleation enhancement from hydrogen. The calculation was also very simplified, involving many approximations, but it indicated that this pinning point formation probability would

increase greatly with tension for most concentrations and temperatures, and that its strain dependence increased for lower temperatures. There was some variation at the highest concentration, when the concentration difference between strained regions became small; this meant that the increased kink-trapping energy of hydrogen in compressive areas became dominant in determining the effect, so that the trend was reversed. The lowest concentration calculated also showed some variation in that the effect of hydrogen was so low that the effects of temperature became dominant: the pinning-point chance was then determined by the increased phonon-drag and thermally activated kink-pair nucleation. In this case the effects of hydrogen across the strains became fairly constant.

Altogether these results indicate that the effect of the same bulk concentration of hydrogen could be very different between regions of tension and compression: the required bulk concentration for significant kink-pair nucleation enhancement would be much lower in regions of tension, and so softening could be entirely localised to those regions. The required bulk concentration for significant pinning-point formation would also be much lower in regions of tension, and so there may be concentrations at which there is significant hardening in tensile regions but significant softening in unstrained or compressive regions; this implies that the region of likely shear localisation could change completely with hydrogen concentration and temperature.

A principal purpose for these simulations was to provide input for the kMC model used by Katzarov et al. [20] to predict the effect of hydrogen on the screw dislocation velocity. Our predictions involve many approximations and also are based on a snapshot of a straight dislocation with no surrounding microstructure. The kMC model would instead allow a realistic description of how the dislocation would evolve, which could alter these effects greatly, and produce more quantitative results. The rates of the kink-pair nucleation, the movement of the kinks and their escape from hydrogen-traps as a function of the stress and temperature are inputs to the kMC model; kinks are allowed to nucleate on any of the three {110} glide planes intersecting the screw ⟨111⟩ slip direction. The collision of crossed-kinks to form immobile jogs is also included in the kMC model, forming strong pinning points on the dislocation line. The kMC model is limited by its input: data from the literature was required to produce these rates and so the model could not be applied to environments for which these hydrogen interactions had not already been calculated.

The results produced here represent almost all of the data required to extend this model to describe the effects of hydrogen on screw dislocation mobility in the strained region surrounding a crack-tip. However, these results cannot be used until the effect of strain on the kink-pair nucleation rate has been calculated.

Acknowledgements

We would like to thank Ivaylo Katzarov for suggesting the problem and for many valuable insights. We acknowledge the support of EPSRC under the Programme Grant HEmS, EP/L014742. We are grateful to the UK Materials and Molecular Modelling Hub for computational resources, which is partially funded by EPSRC (EP/P020194/1), and the ARCHER UK National Supercomputing Service (http://www.archer.ac.uk).

REFERENCES

[1] Brandon NP, Kurban Z. Clean energy and the hydrogen economy. Philosophical Transactions of the Royal Society A 2017;375:20160400. https://doi.org/10.1098/rsta.2016.0400.

[2] Briottet L, Batisse R, Bernard P, Duret-Thual C, Heuzé J-L, Martin F, Thebault F, Vucko F. Industrial consequences of hydrogen embrittlement. Mechanics-Microstructure-Corrosion Coupling. Elsevier; 2019. p. 223–44. https://doi.org/10.1016/B978-1-78548-309-7.50010-7.

[3] Abe J, Ajenifuja E, Popoola O. Hydrogen energy, economy and storage: review and recommendation. Int J Hydrogen Energy 2019. https://doi.org/10.1016/j.ijhydene.2019.04.068.

[4] San Marchi C, Hecht E, Ekoto I, Groth K, LaFleur C, Somerday B, Mukundan R, Rockward T, Keller J, James C. Overview of the DOE hydrogen safety, codes and standards program, part 3: advances in research and development to enhance the scientific basis for hydrogen regulations, codes and standards. Int J Hydrogen Energy 2017;42:7263–74. https://doi.org/10.1016/j.ijhydene.2016.07.014.

[5] San Marchi C, Harris A, Yip M, Somerday BP, Nibur KA. Pressure cycling of steel pressure vessels with gaseous hydrogen. ASME 2012 Pressure Vessels and Piping Conference. American Society of Mechanical Engineers Digital Collection; 2012. p. 835–44. https://doi.org/10.1115/PVP2012-78709.

[6] Alefeld G, Völkl J, editors. Hydrogen in metals I. Springer Berlin Heidelberg; 1978. https://doi.org/10.1007/3-540-08705-2.

[7] Takai K, Shoda H, Suzuki H, Nagumo M. Lattice defects dominating hydrogen-related failure of metals. Acta Mater 2008;56:5158–67. https://doi.org/10.1016/j.actamat.2008.06.031.

[8] Robertson I, Birnbaum H. An HVEM study of hydrogen effects on the deformation and fracture of nickel. Acta Metall 1986;34:353–66. https://doi.org/10.1016/0001-6160(86)90071-4.

[9] Barnoush A, Vehoff H. Recent developments in the study of hydrogen embrittlement: hydrogen effect on dislocation nucleation. Acta Mater 2010;58:5274–85. https://doi.org/10.1016/j.actamat.2010.05.057.

[10] Nagumo M. Hydrogen related failure of steels – a new aspect. Mater Sci Technol 2004;20:940–50. https://doi.org/10.1179/026708304225019687.

[11] Vehoff H, Neumann P. Crack propagation and cleavage initiation in Fe 2.6%-Si single crystals under controlled plastic crack tip opening rate in various gaseous environments. Acta Metall 1980;28:265–72. https://doi.org/10.1016/0001-6160(80)90161-3.

[12] Sofronis P. The influence of mobility of dissolved hydrogen on the elastic response of a metal. J Mech Phys Solid 1995;43:1385–407. https://doi.org/10.1016/0022-5096(95)00037-j.

[13] Ventelon L, Willaime F, Clouet E, Rodney D. *Ab-initio* investigation of the Peierls potential of screw dislocations in BCC Fe and W. Acta Mater 2013;61:3973–85. https://doi.org/10.1016/j.actamat.2013.03.012.

[14] Dezerald L, Ventelon L, Clouet E, Denoual C, Rodney D, Willaime F. *Ab-initio* modeling of the two-dimensional

energy landscape of screw dislocations in BCC transition metals. Phys Rev B 2014;89:024104. https://doi.org/10.1103/physrevb.89.024104.
[15] Rodney D, Ventelon L, Clouet E, Pizzagalli L, Willaime F. Ab initio modeling of dislocation core properties in metals and semiconductors. Acta Mater 2017;124:633–59. https://doi.org/10.1016/j.actamat.2016.09.049.
[16] Zhao Y, Lu G. QM/MM study of dislocation—hydrogen/helium interactions in α-Fe. Model Simulat Mater Sci Eng 2011;19:065004. https://doi.org/10.1088/0965-0393/19/6/065004.
[17] Itakura M, Kaburaki H, Yamaguchi M, Okita T. The effect of hydrogen atoms on the screw dislocation mobility in BCC iron: a first-principles study. Acta Mater 2013;61:6857–67. https://doi.org/10.1016/j.actamat.2013.07.064.
[18] Fellinger MR, Tan AMZ, Hector LG, Trinkle DR. Geometries of edge and mixed dislocations in BCC Fe from first-principles calculations. Physical Review Materials 2018;2:113605. https://doi.org/10.1103/physrevmaterials.2.113605.
[19] Paxton AT, Elsässer C. Electronic structure and total energy of interstitial hydrogen in iron: tight-binding models. Phys Rev B 2010;82:235125. https://doi.org/10.1103/physrevb.82.235125.
[20] Katzarov IH, Pashov DL, Paxton AT. Hydrogen embrittlement I. Analysis of hydrogen-enhanced localized plasticity: effect of hydrogen on the velocity of screw dislocations in α-Fe. Physical Review Materials 2017;1:033602. https://doi.org/10.1103/physrevmaterials.1.033602.
[21] Sutton AP, Finnis MW, Pettifor DG, Ohta Y. The tight-binding bond model. J Phys C Solid State Phys 1988;21:35–66. https://doi.org/10.1088/0022-3719/21/1/007.
[22] Foulkes WMC, Haydock R. Tight-binding models and density-functional theory. Phys Rev B 1989;39:12520. https://doi.org/10.1103/PhysRevB.39.12520.
[23] Kohn W, Sham LJ. Self-consistent equations including exchange and correlation effects. Phys Rev 1965;140:A1133–8. https://doi.org/10.1103/physrev.140.a1133.
[24] Harris RA, Pratt LR. A method for systematic inclusion of electron correlation in density functionals. J Chem Phys 1985;83:4024–8. https://doi.org/10.1063/1.449117.
[25] Foulkes WMC. Interatomic forces in solids. PhD Thesis; 1987.
[26] Goodwin L, Skinner AJ, Pettifor DG. Generating transferable tight-binding parameters: application to silicon. Europhys Lett 1989;9:701–6. https://doi.org/10.1209/0295-5075/9/7/015.
[27] Slater JC, Koster GF. Simplified LCAO method for the periodic potential problem. Phys Rev 1954;94:1498–524. https://doi.org/10.1103/physrev.94.1498.
[28] Paxton AT. An introduction to the tight binding approximation—implementation by diagonalisation. In: Grotendorst J, Attig N, Blügel S, Marx D, editors. Multiscale simulation methods in molecular sciences, vol. 42; 2009. p. 145–74. of *NIC series*, Institute for Advanced Simulation, Forschungszentrum Julich. Available online at: http://juser.fz-juelich.de/record/3737/files/nic-series-volume42.pdf.
[29] Mulliken RS. Electronic population analysis on LCAO–MO molecular wave functions. I. J Chem Phys 1955;23:1833–40. https://doi.org/10.1063/1.1740588.
[30] Hellmann H, Deuticke F. Einführung in die quantenchemie: Texte imprimé. 1937. https://doi.org/10.1007/978-3-662-45967-6.
[31] Feynman RP. Forces in molecules. Phys Rev 1939;56:340–3. https://doi.org/10.1103/physrev.56.340.
[32] Paxton AT, Finnis MW. Magnetic tight binding and the iron-chromium enthalpy anomaly. Phys Rev B 2008;77. https://doi.org/10.1103/physrevb.77.024428.
[33] Finnis MW, Paxton AT, Methfessel M, van Schilfgaarde M. Self-consistent tight-binding approximation including polarisable ions. MRS Proceedings 1997;491. https://doi.org/10.1557/proc-491-265.
[34] Finnis MW, Paxton AT, Methfessel M, van Schilfgaarde M. Crystal structures of zirconia from first principles and self-consistent tight binding. Phys Rev Lett 1998;81:5149–52. https://doi.org/10.1103/PhysRevLett.81.5149.
[35] Stoner EC. Collective electron ferromagnetism II. Energy and specific heat. Proc Roy Soc Lond A 1939;169:339–71. https://doi.org/10.1098/rspa.1939.0003.
[36] Gröger R, Bailey AG, Vitek V. Multiscale modeling of plastic deformation of molybdenum and tungsten: I. Atomistic studies of the core structure and glide of 1/2<111> screw dislocations at 0K. Acta Mater 2008;56:5401–11. https://doi.org/10.1016/j.actamat.2008.07.027.
[37] Fletcher R, Powell MJD. A rapidly convergent descent method for minimization. Comput J 1963;6:163–8. https://doi.org/10.1093/comjnl/6.2.163.
[38] Methfessel M, Paxton AT. High-precision sampling for Brillouin-zone integration in metals. Phys Rev B 1989;40:3616–21. https://doi.org/10.1103/physrevb.40.3616.
[39] Jiang DE, Carter EA. Diffusion of interstitial hydrogen into and through BCC Fe from first principles. Phys Rev B 2004;70:064102. https://doi.org/10.1103/physrevb.70.064102.
[40] Kolos W, Roothaan CCJ. Accurate electronic wave functions for the H_2 molecule. Rev Mod Phys 1960;32:219–32. https://doi.org/10.1103/revmodphys.32.219.
[41] Gibala R, Counts WA, Wolverton C. The hydrogen cold work peak in bcc iron: revisited, with first principles calculations and implications for hydrogen embrittlement. Mater Res 2018;21. https://doi.org/10.1590/1980-5373-mr-2017-0868.
[42] Ramasubramaniam MIA, Carter EA. Interatomic potentials for hydrogen in α-iron based on density functional theory. Phys Rev B 2009;79:174101. https://doi.org/10.1103/physrevb.79.174101.
[43] Ramasubramaniam A, Itakura M, Ortiz M, Carter E. Effect of atomic scale plasticity on hydrogen diffusion in iron: quantum mechanically informed and on-the-fly kinetic Monte Carlo simulations. J Mater Res 2008;23:2757–73. https://doi.org/10.1557/jmr.2008.0340.
[44] Hirth JP. Effects of hydrogen on the properties of iron and steel. Metallurgical Transactions A 1980;11:861–90. https://doi.org/10.1007/bf02654700.
[45] Hirth JP, Lothe J. Theory of Dislocations. 2nd ed. New York: McGraw-Hill; 1982.
[46] Ventelon L, Willaime F, Leyronnas P. Atomistic simulation of single kinks of screw dislocations in α-Fe. J Nucl Mater 2009;386–388:26–9. https://doi.org/10.1016/j.jnucmat.2008.12.053.
[47] Deo WCC, Srolovitz D, Bulatov V. Stochastic simulation of dislocation glide in tantalum and Ta-based alloys. J Mech Phys Solid 2005;53:1223–47. https://doi.org/10.1016/j.jmps.2005.01.003.
[48] Kuksin AY, Yanilkin AV. Atomistic simulation of the motion of dislocations in metals under phonon drag conditions. Phys Solid State 2013;55:1010–9. https://doi.org/10.1134/s1063783413050193.
[49] Itakura M, Kaburaki H, Yamaguchi M. First-principles study on the mobility of screw dislocations in BCC iron. Acta Mater 2012;60:3698–710. https://doi.org/10.1016/j.actamat.2012.03.033.
[50] Caillard D. Kinetics of dislocations in pure Fe. part I. in situ straining experiments at room temperature. Acta Mater 2010;58:3493–503. https://doi.org/10.1016/j.actamat.2010.02.023.
[51] Weinan E, Ren W, Vanden-Eijnden E. String method for the study of rare events. Phys Rev B 2002;66:052301. https://doi.org/10.1103/physrevb.66.052301.